Iron Nanoparticle Generation by He⁺ Ion Bombardment

Fernando Pomiro,*,[†] Adriana E. Candia,[†] Silvia Montoro,[†] Mario C. G. Passeggi, Jr.,[†,‡] Gustavo Ruano,*,[†] and Julio Ferrón[†,‡]

[†]Instituto de Física del Litoral (Universidad Nacional del Litoral-CONICET), Güemes 3450, S3000GLN Santa Fe, Argentina

[‡]Departamento de Materiales, Facultad de Ingeniería Química, Universidad Nacional del Litoral, Santiago del Estero 2829, S3000AOM Santa Fe, Argentina

Ⓢ *Supporting Information*

ABSTRACT: The effect of (1−4 keV) energetic He⁺ ion irradiation over clean pyrite substrates was studied by means of a multitechnique approach, including scanning tunneling microscopy (STM), scanning tunneling spectroscopy (STS), X-ray photoelectron spectroscopy (XPS), ion scattering spectrometry (ISS), and Auger electron spectroscopy (AES). Using these different techniques, we were able to characterize with a great amount of detail the nanostructuring process. Thus, meanwhile through STM we found that upon ion irradiation the surface becomes structured with particles in the nanometer range; through XPS and ISS we determined that these particles are mostly composed of metallic iron. Through STM we also found that surface roughness increases with ion energies, and using oxygen as a marker, we characterize through AES the in-depth iron distribution. Finally, through STS we found changes in the pyrite band gap induced by ion bombardment.
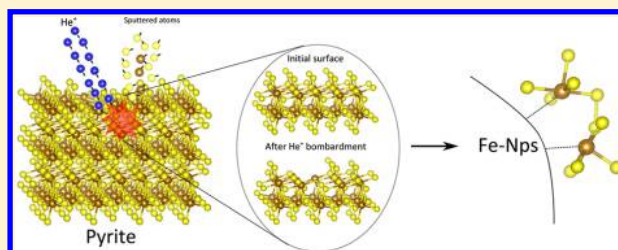
1. INTRODUCTION

The modification of matter through ion bombardment has been a matter of interest for decades, with applications on surface hardness, resistance to corrosion, improvement of adhesion, and so on.[1−5] Thus, ion based bombardment techniques are nowadays applied on a wide range of areas such as food, medicine, aircraft, automobile production, etc. Recently, a renewed interest in these techniques has been triggered by their possible applications on surface nanostructure developments. For instance, the self-assembled nanostructure formation following mild energetic ion bombardment represents a new and exciting area of ion bombardment applications.[4,5]

Ion induced chemical reactions are another way of using mild energy ion bombardment to induce surface structures. For instance, Leibsle et al.[6] found that the mild annealing of a Cu(001) sample, implanted with low energy N⁺ ions, gives place to a self-organized square-shaped nanostructure characterized by a c(2 × 2) N−Cu structure, with a lattice parameter of 4 Å. With the controlled fabrication of nanostructures with application in magnetic recording media, tunnel junctions, and magnetic-random access memories, a leading idea in this field, the creation of magnetic nanostructures using Leibsle's nanostructures as a template seems to be a good idea at first sight. Attempts in this sense have been made, by growing Co and Fe films over N−Cu(001).[7,8]

With an interest in understanding the effect of solar wind on iron compounds, we found that He⁺ ion bombardment reduces the Fe²⁺ contained in a pyrite crystal (FeS₂) into metallic iron.[9] Additionally, it is already known that ion bombardment leads to the generation of S vacancies in pyrite surfaces.[10−12] Both these

results encourage us to test this system as a playground for the bottom-up production of nanostructured aggregates. From the applied point of view pyrite is an ideal material; it is a cheap and naturally abundant mineral, diamagnetic and semiconducting in its native form. Additionally, this method could provide us with metallic particles directly embedded in the semiconductor matrix. Although our interest aims to gain knowledge about the physics involved in basic mechanisms, the technological interest in the generation of nanometallic domains implanted in a semiconductor matrix is undeniable. In this work, we focused our interest in determining the morphology (either film or segregated particles) and distribution of reduced iron within the FeS₂ matrix and the changes in the local electronic structure of the pyrite surface due to He⁺ ion bombardment at low kinetic energies (1−4 keV). With this purpose, we performed a multitechnique analysis of irradiated samples that includes scanning tunneling microscopy (STM), scanning tunneling spectroscopy (STS), X-ray photoelectron spectroscopy (XPS), ion scattering spectrometry (ISS), and Auger electron spectroscopy (AES).
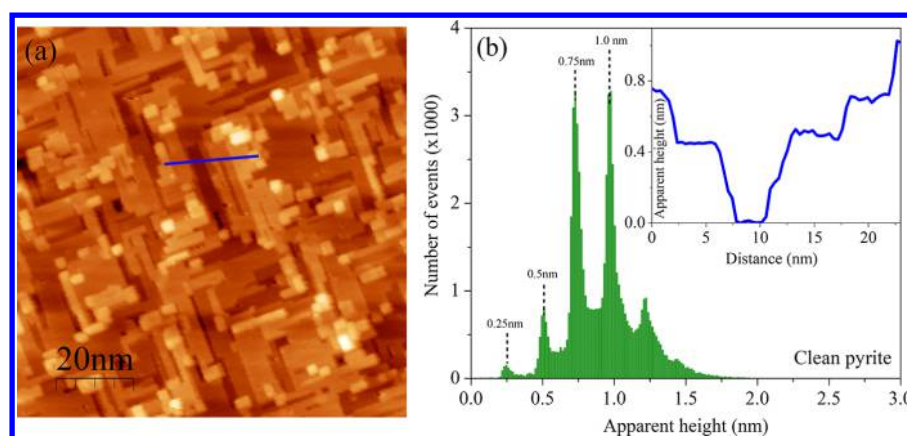
2. EXPERIMENTAL SECTION

2.1. Cleaning Procedure of Pyrite Surfaces. The pyrite samples were natural crystals provided by Manchester Minerals, UK. The crystals were cut into plates of 1 × 1 × 0.01 cm³ in such a way that one side exposes the as-grown surface ((001)

Figure 1. (a) Topographic STM image (100 nm × 100 nm) of a clean pyrite sample (the full z scale is 2 nm). The image was acquired with a sample bias voltage of V_{sp} = +0.55 V and a tunnel current of I_{sp} = 0.08 nA. (b) An apparent height histogram obtained from image a; inset shows an apparent heights profile scan acquired along the line depicted in part a.

plane).[13] A pretreatment of a 20 min immersion in ethanol, in an ultrasonic bath, was applied to degrease the surface. The sample was carefully handled to avoid any mechanical or chemical alteration of the natural surface outside the experimental chamber. Inside the ultrahigh vacuum (UHV) chamber, the pyrite sample was cleaned following the method recently proposed by Sanchez-Arenillas et al.[14] The surface was bombarded during 10 min with 500 eV Ar^+ ions and annealed at 600 K for 4 h. Surface cleanliness was monitored by AES and XPS techniques. The pyrite sample was never overheated beyond 600 K to avoid thermal decomposition. The Ar^+ beam impinged the surface at an angle of 54°, and the ion current densities were kept at 1.5 μA/cm^2, which corresponds to a total dose of 7 × 10^{14} ions/cm^2.

2.2. Sample Modification. The clean pyrite surface was modified by He^+ ion current densities of 12 μA/cm^2 at 1, 2, 3, and 4 keV. The He^+ ion beam was maintained over the surface, with a total ion dose of 8 × 10^{15} ions/cm^2. The ion gun was unfiltered using 5N pure He gas. In this case, the impinging angle was perpendicular to the pyrite surface.

2.3. Characterization Techniques. *2.3.1. Auger Electron Spectroscopy.* AES measurements were performed in a commercial UHV surface analysis system with a base pressure in the 10^{-10} mbar range. Differentiated Auger spectra of the O_{KLL}, C_{KLL}, $S_{L2,3VV}$, $Fe_{M2,3VV}$, and Fe_{LMM} transitions were acquired using a single-pass cylindrical mirror analyzer (CMA) with a resolution of 0.3%, 2 V_{p-p} modulation amplitude, step energy of 0.5 eV, and dwell time of 0.25 s. The incidence angle of the electron beam was 30° with respect to the surface normal, and the excitation energy employed was 3 keV. The depth profiling was performed using 500 eV Ar^+ ions, and the beam impinged the surface at an angle of 54° with ion current densities of 2 μA/cm^2.

With the goal of this work being the interaction of charged kinetic particles, such as He^+ ions, with pyrite surfaces, in the first place we checked if the sample undergoes any degradation process under electron bombardment in the AES experiments. In order to perform it, we took continuous AES spectra for 6 h. No changes in the line shape or intensity of either Fe or S were observed, confirming in this way that electron beam damage is negligible under our experimental conditions.

2.3.2. X-ray Photoelectron Spectroscopy and Ion Scattering Spectrometry. XPS and ISS experiments were done in an SPECS system with a base pressure in the range of low 10^{-10}

mbar, equipped with a hemispherical energy analyzer, a differentially pumped mass analyzed ion gun, and a double anode X-ray source. The XPS data were collected after exciting the sample by an Al Kα line at 1486.6 eV. XPS spectra were acquired using a constant analyzer energy of 20 eV, with energy steps of 0.05 eV and a dwell time of 0.33 s. The ISS measurements were performed using a 2 keV He^+ beam with a scattering angle of 125°. During the experiment, in which the ions are used both for changing and probing the sample, the ion density current was set at 0.2 μA/cm^2. In both systems the sample can be heated by electron rear bombardment and the temperature controlled by a chromel−alumel thermocouple.

2.3.3. Scanning Tunneling Microprobe. 2.3.3.1. Scanning Tunneling Microscopy. The STM measurements were performed at room temperature in an UHV chamber with a base pressure in the low 10^{-10} mbar range. The sample was cleaned in a secondary UHV chamber attached to the main one. A chromel−alumel thermocouple, attached to the backside of the sample holder, was used to measure its temperature. Vacuum conditions in the secondary chamber were kept in the 10^{-9} mbar range. Electrochemical etched tungsten tips were used for all STM experiments reported in this work. The polycrystalline W tips were routinely cleaned by Ar^+ ion bombardment in UHV. All the STM images obtained in this study were acquired in the constant current mode with positive sample bias voltages, between +0.3 and 1.7 V. The tunneling currents used were in the range between 0.07 and 0.2 nA. Acquisition and image processing were performed using the WS×M free software.[15]

2.3.3.2. Scanning Tunneling Spectroscopy. As usual, to acquire current−separation *I−S* or current−bias *I−V* curves, the feedback loop was turned off for a few microseconds. The *I−V* curves were taken over a zone of 20 nm × 20 nm^2 (atomically flat for the case of clean pyrite). All *I−V* curves shown in this work represent the average of 30 reproducible measurements without changing the lateral position, the tip−sample distance, and the potential sweep rate. The STS curves were measured at various tip−sample separation distances (*s*). In order to do this, *I−S* curves were acquired varying V_{sp} between −2 and 2 V and keeping the I_{sp} constant at 1 nA. All of the *I(s)* curves in this study represent an average over approximately 10 measurements at different points on the pyrite surface. To obtain reliable information from *I−V* curves we follow the normalization procedure suggested by Herbert et
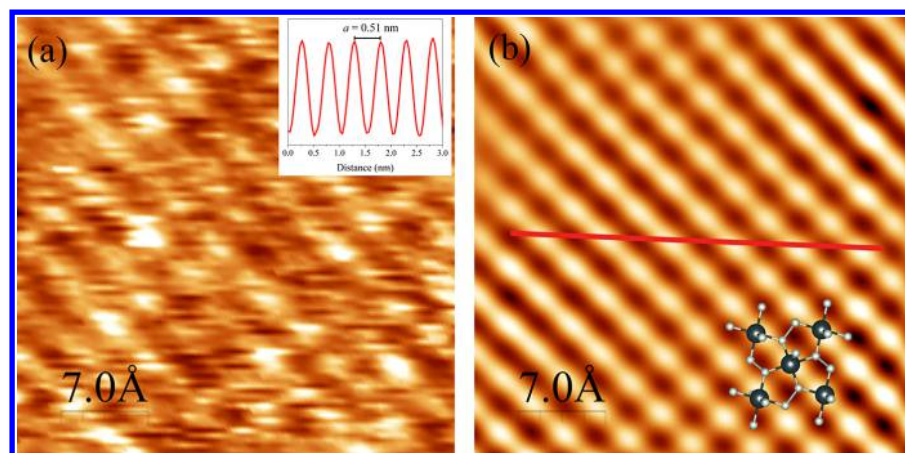
Figure 2. (a) Current STM image (3.5 nm × 3.5 nm) with atomic resolution obtained over a terrace of the image shown in Figure 1a. The images were acquired at V_{sp} = +0.18 V and I_{sp} = 1.8 nA. (b) As a low pass filtered image obtained performing a 2D-FFT to image a, the face centered cubic unit cell for pyrite is shown (Fe in black, S in white). Inset shows a profile scan against distance acquired along the line depicted in part b, showing an average of the pyrite unit cell parameter.

al.[16] The application of this method to our experiments can be followed in the Supporting Information.

3. RESULTS AND DISCUSSION

In Figures 1 and 2, we show a complete STM characterization of the clean pyrite surface. The negligible amounts of C and O detected by AES (see Figure S1 in the Supporting Information), together with the minimal roughness, are comparable to those obtained for UHV freshly cleaved pyrite by Rosso et al.,[17] which gives strong support to the Sanchez-Arenillas et al.[14] method for being used as a pyrite cleaning procedure.

In Figure 1a, we depict a (100 nm × 100 nm) topographic STM image of a clean pyrite surface. The image is dominated by rectangular flat terraces, which are oriented along the crystallographic symmetry axis of the sample. These terraces are mostly terminated by half of a unit cell step-edge (0.25 nm), as can be observed in the apparent heights histogram and profile depicted in Figure 1b, and in its inset. Taking a look at these histograms, we can clearly identify the representative peaks of a six stepped height surface. The equal distribution among both of these two kinds of terraces suggests that they are thermodynamically equivalent.

After completing all of the sputter/annealing cycles, we acquired images with atomic resolution like those depicted in Figure 2, concluding that the local morphology is not affected during the cleaning procedure. In Figure 2b, we show an improved image of Figure 2a by doing a low pass filtered procedure, where the top layer Fe-localized states are observed at the corners of the pyrite unit cell.[18−20] Note that thermal and piezoelectric drift was substantial during imaging of Figure 2a, which caused a distortion in the square surface unit cell in the vertical direction. The cubic centered unit cell for pyrite is clearly distinguished in the atomic resolution filtered image (Figure 2b), and the atomic distance among Fe cations can be determined following the line profile depicted in Figure 2b, and drawn in the inset of Figure 2a.

Once the pyrite surface is adequately prepared and characterized, we proceed with our experiment. In Figure 3 we summarize the results for the surface topography evolution under He$^+$ ion bombardment for energies from 1 to 4 keV. In this figure we depict topography STM images, after 1 min of
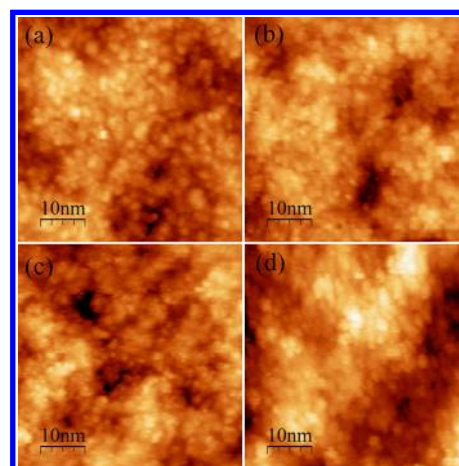

Figure 3. Topographic STM images (50 nm × 50 nm) of a pyrite sample bombarded with He$^+$ ions of (a) 1, (b) 2, (c) 3, and (d) 4 keV. The images were acquired at V_S = +0.80, +0.60, +0.70, +1.70 V and I_T = 0.20, 0.08, 0.08, 0.09 nA, respectively.

He$^+$ bombardment (8×10^{15} ions/cm^2) at 1, 2, 3, and 4 keV (a, b, c, and d, respectively) of kinetic energy. The formation of nanoparticles under ion bombardment is quite apparent along this series of images.

In order to quantify this result, we show in Figure 4 the evolution of the roughness with ion energy, and the frequency of occurrence of the different terrace apparent heights. The root-mean-square (RMS) of the roughness values for the different ion energies are obtained through a series of 3 or more (100 nm × 100 nm) images acquired during each energy experiment. A clear, almost linear, increase of the RMS of the roughness with the ion bombarding energy is observed (see inset of Figure 4).

The results depicted in Figures 3 and 4 show startling changes generated in the surface topography by He$^+$ ion bombardment. The increase in the surface roughness is accompanied by a general change of the surface morphology, with the disappearance of terraces and steps. The bombarded surface is characterized by a rather uniform distribution of nanoparticles. The maximum apparent heights of particles, as well as their apparent height dispersion, increase with ion
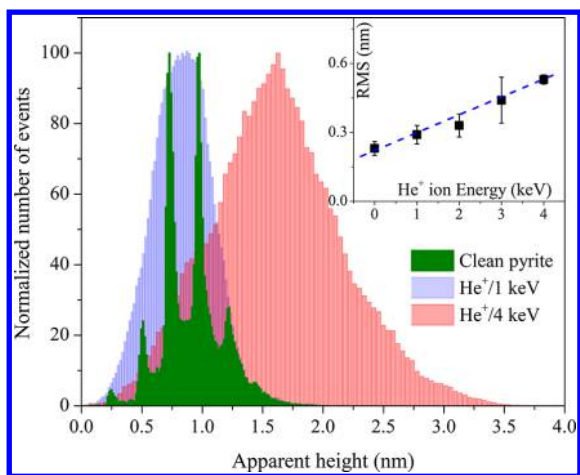
Figure 4. Apparent heights histogram obtained from images in Figures 1a and 3a,d. Inset shows RMS of the roughness values as a function of the different ion bombardment energies.

energy (see Figure 4). The formation of these structures clearly requires an important amount of material diffusion, since the pure and lonely effect of ion bombardment would be the appearance of an amorphous surface, characterized by vacancies and hillocks. To this point, through our STM measurements we can report the formation of nanoparticles, whose size is ion energy dependent. It is clear that, in order to understand and quantify the full process, other parameters like ion incidence angle, ion dose, as well as target surface temperature, either during the bombardment or due to a postannealing process, should be studied in depth. Throughout the rest of this work, we will focus on the study of the chemical composition of these nanoparticles, as well as their in-depth distribution.

Let us first determine the chemical composition of the very surface. In Figure 5 we show the characterization of the pyrite
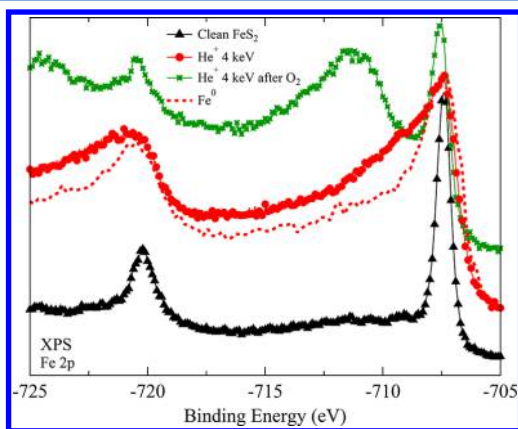
Figure 5. XPS yields obtained for clean FeS_2 (pyrite), bombarded with He^+ of 4 keV and after a postoxidation process. A pure metallic Fe spectrum is also shown.

surface, restricted to the iron evolution, using XPS for a particular subset of our full experiment. The evolution of Fe and S compounds under bombardment, as well as the subsequent oxidation process, has been studied in detail combining XPS with factor analysis.[9] In this article, in Figure 5, we depict just the results that show the formation of metallic iron induced by He^+ bombardment, and its full oxidation after exposure to atmospheric condition. The XPS results, shown in

Figure 5 for pristine pyrite, 4 keV He^+ bombarded pyrite, the postoxidized sample, and the pure metallic iron sample, clearly show the reduction of Fe^{2+} due to ion bombardment. Indeed, with a comparison of the bombarded pyrite spectrum with that of pure metallic iron, we can clearly observe the broadening of the Fe 2p line shape corresponding to the pyrite peak, which can be taken as a fingerprint of the reduction process. The XPS spectrum obtained after the oxidation process shows both the disappearance of the metallic peak and the appearance of the characteristic iron oxide peak.[21] In summary, results depicted in Figure 5 show the reduction of Fe^{2+} in FeS_2, through the appearance of the Fe^0 characteristic peak, and the full oxidation of Fe through the exposure to oxygen.

As much as XPS is a surface sensitive technique, it is clear that while STM is actually observing the top-most surface, the XPS analyzed volume extends some nanometers in depth. A technique that is able to give information on the very same surface region as STM is indeed ion scattering spectrometry (ISS). In Figure 6a we show a subset of ISS spectra in the region of the He−Fe (peak at 1540 eV) and He−S (at 1390 eV) binary collisions, and in panel b the count number evolution for both cases as the He^+ bombardment proceeds. The results clearly show that there is a preferential depletion of S at the surface, as the sputtering process proceeds. This directly turns into changes in the surface composition, shown in Figure 6c, where we observe a monotonous decrease with the He^+ dose reaching a total S depletion of the outermost surface. In this figure, we have assumed that the maximum ratio at the initial instances of the bombardment corresponds to a 2:1, S to Fe ratio. This result itself constitutes an independent piece of evidence for the ion induced Fe reduction. Although ISS is not a chemical sensitive technique, as XPS is, the total depletion of S from the surface is undoubtedly a direct proof of the iron reduction.

From STM measurements we have determined topographical changes of the pyrite surface induced by ion bombardment, including the formation of particles of nanometer size. From ISS we can determine, through a physical process, that the outermost layer is formed by pure iron. At the same time, determining the chemical shifts with XPS, we can be quite sure that the formation of metallic iron due to He^+ ion bombardment extends to a certain depth. The question then is related to the extension of this reduced/damaged zone within the sample. To gain information about this point, we used a technique with larger surface sensitivity than XPS, low energy like AES. Indeed, the use of the low energy peak of iron ($Fe_{M2,3VV}$: ~50 eV) fits our spatial resolution requirements. In this way, we have a technique more (less) surface sensitive than XPS (ISS) but, at the same time, with a better (worse) chemical selectivity than ISS (XPS). With a combination of this low Auger energy analysis with swift Ar^+ ion bombardment, we can obtain a more accurate in-depth distribution of reduced iron.

Although the AES capability for chemical identification is far from that of XPS, this does not mean that no useful information can be derived from the line shape analysis of the different Auger signals. In Figure 7a,b, we depict the $Fe_{M2,3VV}$ and $S_{L2,3VV}$ AES lines, respectively, corresponding to pyrite bombarded with 4 keV He^+ and then exposed to oxygen. The idea of working with the postoxidized sample is just to enhance the chemical sensitivity of AES. Since from XPS measurements we have determined (Figure 5) that iron is fully oxidized after the oxygen exposure, determining that the oxidized iron distribution will be equivalent to determining the
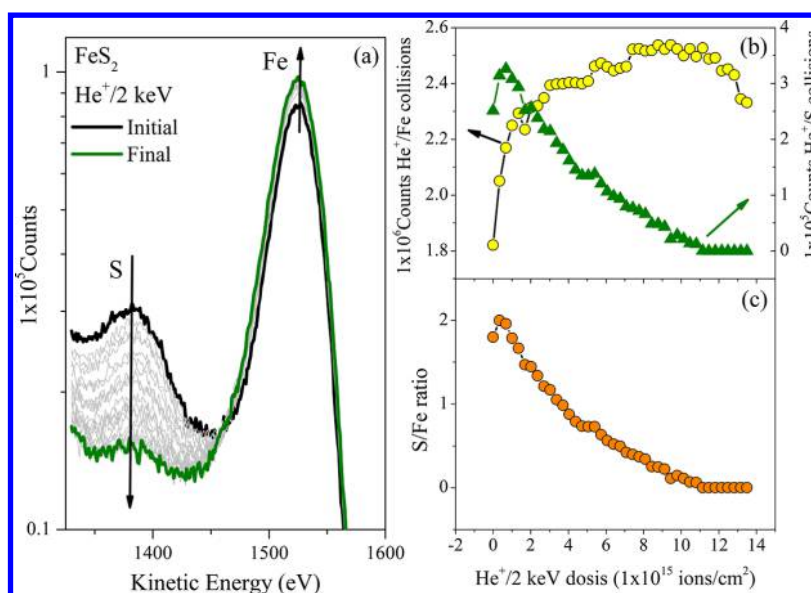
Figure 6. (a) Subset of ISS spectra in the region of the He–Fe (1540 eV) and He–S (1390 eV) binary collision, (b) count number evolution for both cases, and (c) S/Fe ratio along the He$^+$ bombardment process.
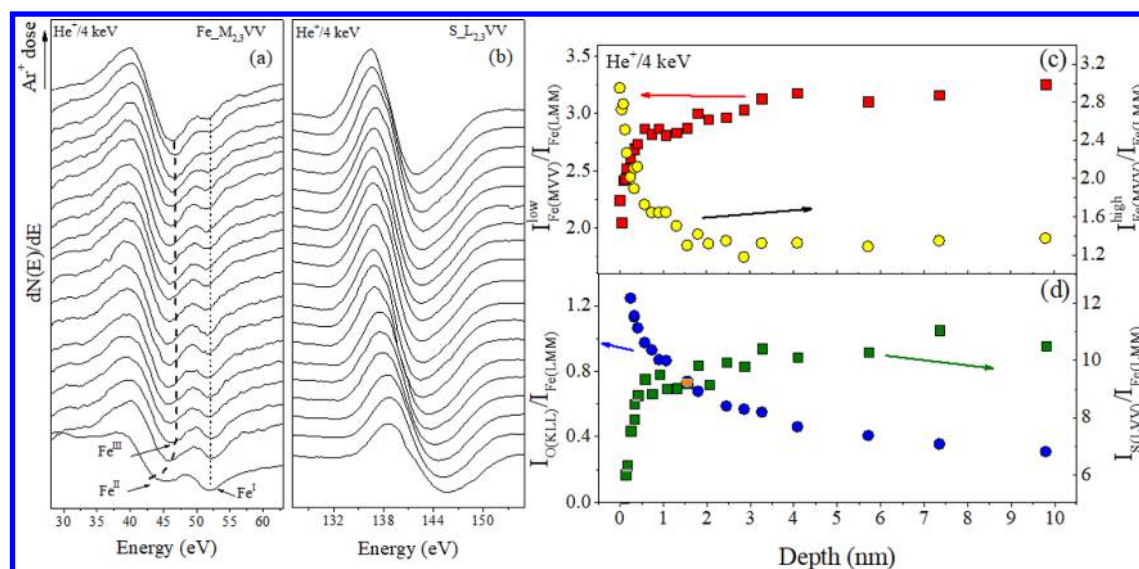
Figure 7. (a) Fe$_{M2,3VV}$ and (b) S$_{L2,3VV}$ AES signal evolution (for different 500 eV Ar$^+$ ion bombarding doses) corresponding to pyrite bombarded with He$^+$ 4 keV and then exposed to oxygen. In-depth evolutions of the normalized intensities of (c) both structures of the Fe$_{M2,3VV}$ signal and (d) S$_{L2,3VV}$ and O$_{KLL}$ Auger transitions.

metallic iron one. The evolution (from bottom to top, Figure 7a,b) corresponds to different 500 eV Ar$^+$ ion bombarding doses, and thus to increasing depths into the subsurface. Similar sets of spectra were acquired for the other (three) analyzed regions.

The Fe$_{M2,3VV}$ Auger line shape is characterized by two peaks along the full depth profile. While the energy of one of these peaks remains almost unchanged at 52 eV (Fe^I), the other one moves from 44.5 (Fe^{II}) to 46.5 eV (Fe^{III}), just after a very low ion bombarding dose has been applied. This evolution is similar to the one reported by Seo et al.[22] for the depth profile of an iron oxide film (90% Fe$_3$O$_4$ and 10% α-Fe$_2$O$_3$) grown on metallic Fe. They assigned the first structure (Fe^I and Fe^{II}) to Fe^{3+} (Fe$_2$O$_3$) and the other one, appearing after a mild bombardment (Fe^I and Fe^{III}), to a mixture of Fe^{2+} and Fe^{3+}, like the one existing in magnetite (Fe$_3$O$_4$). In our case, we

assign this structure to a mixture of magnetite and pyrite. To support our suggestion, one can follow the different relative weights of low and high energy Fe peaks of these compounds, shown in Figure 7c. As the depth profile progresses, the high energy peaks tend to disappear recovering the Auger line shape of the pristine pyrite.

With regard to the S$_{L2,3VV}$ signal (see Figure 7b), in addition to the increase of the yield due to the changes in sulfur concentration, we observe a narrowing and slight shift to lower energies. This shape evolution is indeed due to changes in the environment, but it cannot be resolved by AES, and we should use XPS instead. After a fast increase, due to surface effects, the S yield reaches along the depth profile two steady state regions, between 1–3 and 4–10 nm in Figure 7d. From Figure 7c,d, we observe that these sulfur regions follow those of oxygen and iron (high energy peak).

Thus, neglecting the fast evolution corresponding to the very surface zone, our results are consistent with two regions of different oxygen/sulfur concentration, and two different iron oxide states. The first one (from 1 to 3 nm) is associated with a mixture of magnetite and pyrite, characterized by a lower (higher) sulfur (oxygen) concentration with an important contribution of the high energy $Fe_{M2,3VV}$ peak, and the last one (beyond 4 nm), corresponding to pure pyrite, with a small amount of O, since then the Auger line shape can be clearly assigned to FeS_2.[23]

One very apparent feature in the S in-depth content, depicted in Figure 7d, is its clear depletion in the surface region. We used this feature to estimate the Ar^+ sputtering coefficient, considering that the S bulk signal becomes attenuated in the oxygen rich outermost layer (blue profile in Figure 7d). We estimate a sputtering rate of 0.03 nm/min for our experimental conditions, which is very consistent with the values obtained, on the basis of TRIM simulations (0.04 nm/min).[24]

Looking at the depth scale in Figure 7c,d, we can conclude that the surface altered region, both due to ion bombardment and after the postoxidation process, is on the same order as the roughness of the surface. Apparently, we can develop nanometer scaled particles, rich in metallic iron, that can be easily oxidized resulting in some mixture of magnetite and pyrite. Better chemical identification can be indeed performed with XPS, and we are currently working on this matter. On the other hand, a more accurate in-depth characterization of the nanostructured surface can be performed by using the oxygen Auger transition as a marker. As we showed in Figure 5, metallic iron is fully oxidized; thus, following the O_{KLL} Auger line along the Ar^+ ion depth profiling will give us the extent of the ion modified surface. We depict these results in Figure 8.
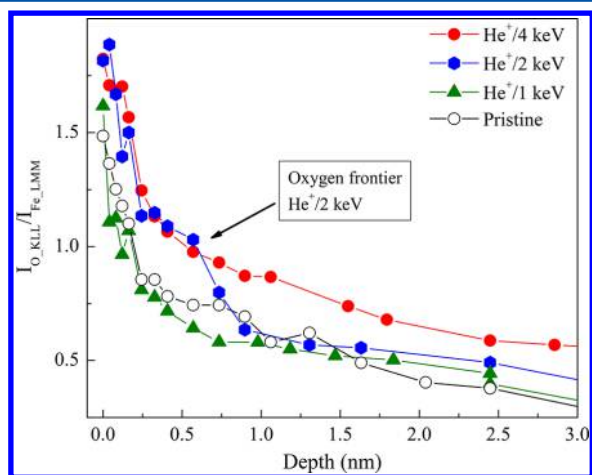
**Figure 8.** In-depth distribution of the O_{KLL} AES signal for pyrite under different irradiation conditions.

In Figure 8 we show the in-depth distribution of Fe^0 by following the oxygen (O_{KLL}) Auger peak through the Ar^+ ion bombarding erosion of the sample. In doing that, four regions in the same pyrite surface were studied. Three of them were bombarded with He^+ ions at 1, 2, and 4 keV, and the remaining one was used as a control (clean pyrite). All regions were then exposed in the main chamber to high purity oxygen over 48 h at a pressure of 10^{-3} mbar. From XPS results (Figure 5) we know that under these conditions metallic Fe fully oxidizes. The line shape of the full set of profiles is characterized by peaking

oxygen content at the surface followed by a content decay, whose slopes depend on the He^+ ion energy. To discard either oxygen diffusion or retroimplantation by Ar^+ ion bombardment,[25,26] it is just enough to look at the control profile.

The extension of the modified (structured) surface obtained from AES depth profiles, either from Fe or S transitions, as well as from the O_{KLL} evolution, agrees quite well with the roughness and, ultimately, with the size of the particles generated at the surface by the He^+ ion bombardment. These results suggest then that energetic He^+ bombardment generates nanoparticles at the surface, rich in metallic iron, and fully oxidized at low oxygen pressure.

Our last step in this work is the electronic characterization of the altered layer at the outermost surface, which will be done using STS. One of the problems in STS, mainly when one tries to compare measurements made over different samples, is the impossibility of defining the same tip−surface distance to compare the different measurements. In a recent work, Herbert et al.[16] proposed a method to overcome this problem, based on measuring $I−V$ curves with different sample bias voltages. In the Supporting Information, we briefly explain the way we applied their method to our case. In Figure 9a,b, we show the $I−V$ curves, and in Figure 9c we depict the results, using the absolute value of I, in a log scale, to emphasize the dependence close to the band gap, as suggested in ref 16.
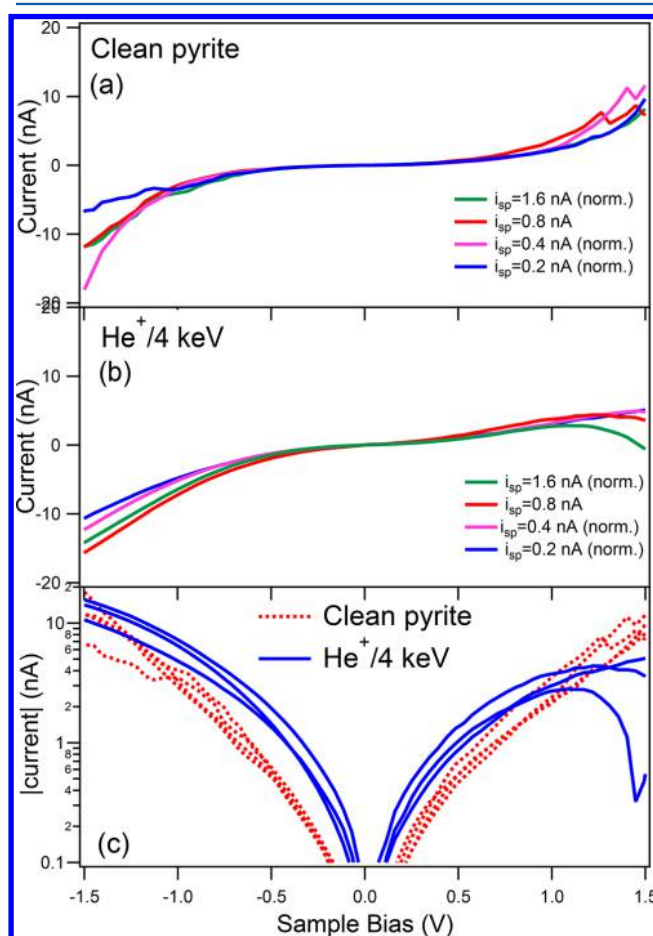
Figure 9. Normalized $I−V$ curves for (a) pristine pyrite and (b) bombarded with 4 keV He^+. (c) Absolute $I−V$ curves for pristine pyrite, and bombarded with 4 keV He^+, in a log scale.

We can observe that although $I-V$ curves were taken with quite different tip–surface distances (determined by the starting I value), once normalized they show quite a similar behavior. For instance, the measurements on pyrite are quite encouraging, since the band gap obtained is close to ~0.5 eV, in good agreement with previous reported works.[16] The $I-V$ curves for the bombarded surface show a larger dispersion than those of pristine pyrite, probably due to the nonbombarded samples presenting smoother and more homogeneous surfaces. However, in spite of these differences, apparently the band gap of the bombarded sample is smaller than that corresponding to the pure semiconductor. It is clear that this is not proof of the surface metallization, since these results could be due to the generation of defects within the band gap, but the point is that the modification of the band gap by bombardment is in the same sense, as suggested by results coming from XPS, ISS, and AES, i.e., the appearance of reduced iron on a film over the surface.

Further investigation of surface annealing is needed in order to observe changes in both the topography, as seen by STM, and the electronics, as seen by STS.

The preferential sputtering of S in the ion bombardment process of pyrite is a well-known fact. For this energy range, another well-known fact is that both the ion range and the vacancy generation cross section increase with ion energy. Thus, it is reasonable to imagine a scenario in which more S vacancies are generated for 4 keV than for 1 keV, and also that they are distributed deeper with respect to the surface.

To explain in full detail the mechanism of iron reduction, i.e., the driving force of chemical reactions on pyrite surface detailed in ref 9, more experiments are required. Nevertheless, an explanation for the ion induced reduction of metal oxides in terms of a thermal spike process was proposed as recently as 1987.[27] In our group, more recently, we found evidence of the existence of electronic excitation driven processes both in HOPG[28] and during the dissociative effusion of hydrogen from nanostructured porous silicon.[29] In this way, exercising some healthy speculation, the ion induced defect states in the pyrite band gap and electronic excitations may induce short-lived energy fluctuations that kick-start the chemical processes.

4. CONCLUSIONS

Our experiments give the following picture for the pyrite samples bombarded with energetic He$^+$ ions.

- STM (1): The pyrite surface treated with mild Ar$^+$ ion bombardment and long annealing periods leads to atomically reconstructed surfaces, terminated in terraces separated by steps half the height of the unit cell.
- STM (2): The bombarded surface is nanostructured. He$^+$ ion bombardment leads to surfaces where steps are erased, and terraces are filled with particles of nanometer size. The roughness of the surface increases almost linearly with energy.
- XPS: The He$^+$ ion bombardment reduces Fe^{2+} from FeS$_2$ to metallic iron. The exposure to atmosphere completely oxidizes the reduced iron.
- AES (1) and Ar$^+$ depth profile: The postoxidized iron, using oxygen (O$_{KLL}$) as a marker, reveals that the metallic iron is compatible with surface roughness.
- AES (2) and Ar$^+$ depth profile: The analysis of Fe$_{M2,3VV}$ and S$_{L2,3VV}$ line shape evolutions gives support to the

analysis based on the oxygen distribution, allowing us to suggest that the oxidized surface contains magnetite.
- ISS: The He$^+$ ion bombardment completely depletes the very surface from sulfur.
- STS: Carefully normalized $I-V$ curves show a clear narrowing of the pyrite band gap induced by He$^+$ ion bombardment.

■ ASSOCIATED CONTENT

Ⓢ Supporting Information

The Supporting Information is available free of charge on the ACS Publications website at DOI: 10.1021/acs.jpcc.7b09361.

AES spectrum of pyrite before and after the cleaning cycles (Ar$^+$ at 500 eV followed by annealing up to 600 K) and explanation of the application of the method used to normalize the $I-V$ curves at different tip–sample distances (PDF)

■ AUTHOR INFORMATION

Corresponding Authors

*E-mail: fernando.pomiro@santafe-conicet.gov.ar.
*E-mail: gustavo.ruano@santafe-conicet.gov.ar. Phone: +54 (342) 455-9174/77 (ext 2100). Fax: +54 (342) 455-0944.

ORCID Ⓘ

Gustavo Ruano: 0000-0001-8035-9061

Notes

The authors declare no competing financial interest.

■ REFERENCES

(1) Ramana, C. V.; Atuchin, V. V.; Becker, U.; Ewing, R. C.; Isaenko, L. I.; Khyzhun, O. Yu.; Merkulov, A. A.; Pokrovsky, L. D.; Sinelnichenko, A. K.; Zhurkov, S. A. Low-Energy Ar$^+$ Ion-Beam-Induced Amorphization and Chemical Modification of Potassium Titanyl Arsenate (001) Crystal Surfaces. *J. Phys. Chem. C* **2007**, *111*, 2702–2708.

(2) Takeuchi, D.; Fukushima, K.; Matsuo, J.; Yamada, I. Study of Ar Cluster Ion Bombardment of a Sapphire Surface. *Nucl. Instrum. Methods Phys. Res., Sect. B* **1997**, *B121*, 493–497.

(3) Pawel, J. E.; Mchargue, C. J.; Wert, J. J. The Influence of Ion Bombardment on the Adhesion of Thin Films to Substrates. *Nucl. Instrum. Methods Phys. Res., Sect. B* **1990**, *B46*, 392–396.

(4) Facsko, S.; Bobek, T.; Kurz, H.; Dekorsy, T.; Kyrsta, S.; Cremer, R. Ion-Induced Formation of Regular Nanostructures on Amorphous GaSb Surfaces. *Appl. Phys. Lett.* **2002**, *80*, 130–132.

(5) Teichert, C. Self-Organization of Nanostructures in Semiconductor Heteroepitaxy. *Phys. Rep.* **2002**, *365*, 335–432.

(6) Leibsle, F. M. Nanostructure Fabrication on Copper Surfaces. *Surf. Sci.* **2002**, *514*, 33–40.

(7) Komori, F.; Lee, K. D.; Nakatsuji, K.; Iimori, T.; Cai, Y. Q. Growth and Magnetism of Co Nanometer-Scale Dots Squarely Arranged Ona. *Phys. Rev. B: Condens. Matter Mater. Phys.* **2001**, *63*, 214420.

(8) Ohno, S.; Nakatsuji, K.; Komori, F. Growth Mechanism of Fe Nanoisland Array on Cu(001)-c(2 × 2)N Surfaces. *Surf. Sci.* **2003**, *523*, 189–198.

(9) Ruano, G.; Pomiro, F.; Ferrón, J. Surface Chemical Reactions Induced on Pyrite by Ion Bombardment. *Surf. Sci.* **2018**, *667*, 138−147.

(10) Chaturvedi, S.; Katz, R.; Guevremont, J.; Schoonen, M. A. A.; Strongin, D. R. XPS and LEED Study of a Single-Crystal Surface of Pyrite. *Am. Mineral.* **1996**, *81*, 261−264.

(11) Guevremont, J. M.; Strongin, D. R.; Schoonen, M. A. A. Effects of Surface Imperfections on the Binding of CH_3OH and H_2O on $FeS_2(100)$: Using Adsorbed Xe as a Probe of Mineral Surface Structure. *Surf. Sci.* **1997**, *391*, 109−124.

(12) Andersson, K.; Nyberg, M.; Ogasawara, H.; Nordlund, D.; Kendelewicz, T.; Doyle, C. S.; Brown, G. E.; Pettersson, L. G. M.; Nilsson, A. Experimental and Theoretical Characterization of the Structure of Defects at the Pyrite $FeS_2(100)$ Surface. *Phys. Rev. B: Condens. Matter Mater. Phys.* **2004**, *70*, 195404.

(13) Moslemzadeh, N.; Tamara, M.; Raval, R.; Prior, D.; Preston, M. R. Improved Efficiency of the Sputtering Technique for Pyrite Surface and Its Effect on Reduction of Electron Beam Damage. *Surf. Interface Anal.* **2009**, *41*, 1−5.

(14) Sanchez-Arenillas, M.; Mateo-Marti, E. Pyrite Surface Environment Drives Molecular Adsorption: Cystine on pyrite(100) Investigated by X-Ray Photoemission Spectroscopy and Low Energy Electron Diffraction. *Phys. Chem. Chem. Phys.* **2016**, *18*, 27219−27225.

(15) Horcas, I.; Fernández, R.; Gómez-Rodríguez, J. M.; Colchero, J.; Gómez-Herrero, J.; Baro, A. M. WSXM: A Software for Scanning Probe Microscopy and a Tool for Nanotechnology. *Rev. Sci. Instrum.* **2007**, *78*, 013705.

(16) Herbert, F. W.; Krishnamoorthy, A.; Van Vliet, K. J.; Yildiz, B. Quantification of electronic band gap and surface states on FeS2(100). *Surf. Sci.* **2013**, *618*, 53−61.

(17) Rosso, K. M.; Becker, U.; Hochella, M. F. Atomically Resolved Electronic Structure of Pyrite (100) Surfaces: An Experimental and Theoretical Investigation with Implications for Reactivity. *Am. Mineral.* **1999**, *84*, 1535−1548.

(18) Rosso, K.; Becker, U.; Hochella, M. The Interaction of Pyrite (100) Surfaces with O_2 and H_2O: Fundamental Oxidation Mechanisms. *Am. Mineral.* **1999**, *84*, 1549−1561.

(19) Fan, F. R.; Bard, A. J. Scanning Tunneling Microscopy and Tunneling Spectroscopy of n-Type Iron Pyrite (n-FeS_2) single crystals. *J. Phys. Chem.* **1991**, *95*, 1969−1976.

(20) Eggleston, C. M.; Ehrhardt, J.-J.; Stumm, W. Surface Structural Controls on Pyrite Oxidation Kinetics: An XPS-UPS, STM, and Modeling Study. *Am. Mineral.* **1996**, *81*, 1036−1056.

(21) Leveneur, J.; Waterhouse, G. I. N.; Kennedy, J.; Metson, J. B.; Mitchell, D. R. G. Nucleation and Growth of Fe Nanoparticles in SiO2: A TEM, XPS, and Fe L-Edge XANES Investigation. *J. Phys. Chem. C* **2011**, *115*, 20978−20985.

(22) Seo, M.; Lumsden, J. B.; Staehle, R. W. An AES Analysis of Oxide Films on Iron. *Surf. Sci.* **1975**, *50*, 541−552.

(23) Raikar, G. N.; Thurgate, S. M. An Auger and EELS Study of Oxygen Adsorption on FeS_2. *J. Phys.: Condens. Matter* **1991**, *3*, 1931−1939.

(24) Ziegler, J. F.; Ziegler, M. D.; Biersack, J. P. SRIM - The Stopping and Range of Ions in Matter (2010). *Nucl. Instrum. Methods Phys. Res., Sect. B* **2010**, *268*, 1818−1823.

(25) Ferrón, J.; De Bernardez, L. S.; Goldberg, E. C.; Buitrago, R. H. Surface concentration changes in Cu-Zn alloys under ion bombardment. *Appl. Surf. Sci.* **1983**, *17*, 241−248.

(26) Ferrón, J.; Vidal, R. Ion Mixing and Backscattering Effect in AES Depth Profiling. *Appl. Surf. Sci.* **1986**, *27*, 329−337.

(27) Ho, S. F.; Contarini, S.; Rabalais, J. W. Ion-Beam-Induced Chemical Changes in the Oxyanions (MO_y^{n-}) and Oxides (MO_x) Where M = Cr, Mo, W, V, Nb, and Ta. *J. Phys. Chem.* **1987**, *91*, 4779−4788.

(28) Bajales, N.; Cristina, L. J.; Mendoza, S.; Baragiola, R. A.; Goldberg, E. C.; Ferrón, J. Exciton Autoionization in Ion-Induced Electron Emission. *Phys. Rev. Lett.* **2008**, *100*, 227604.

(29) Ruano, G. D.; Ferrón, J.; Arce, R. D.; Koropecki, R. R. Kinetics of Electron Induced Desorption of Hydrogen in Nanostructured Porous Silicon. *Phys. Status Solidi A* **2011**, *208*, 1453−1457.